DIGITAL TWIN OF AN AIRCRAFT LANDING GEAR TO ENHANCE FAILURE ANALYSIS AND MANAGE PREDICTIVE MAINTENANCE

David Yishay Sabag[1], Oleg Yakimenko[2] & Hasib Alian[1]

[1]Israeli Air Force, Tel Aviv, Israel
[2]Naval Postgraduate School, Monterey, California

Abstract

The aviation industry strives to implement innovative technologies to improve aircraft performance, efficiency, and safety. This paper focuses on the development of physics-informed digital twin (DT) of aircraft landing gear (LG) system based on a landing database to take advantage of predictive rather than condition-based maintenance of this system. Specifically, this paper presents the results of the study examining the evolution of wear in the LG joint as a function of aircraft operation environment and shows how to build and use a DT around it. The study involves collection and continuous update of the landing database composed of the time histories of the velocity and acceleration vectors before, at, and right after a touchdown event as recorded by each individual aircraft for the specific flight configuration and weather conditions. These data are then processed to identify and analyse the touchdown and breaking events and eventually converted to loads and moments developing in the LG joints. Finally, based on the detailed wear modelling and results of laboratory experiments to investigate the wear phenomenon in the LG bushings influenced by several parameters, the DT of the LG system calculates the expected wear rate, which allows to significantly reduce a post-flight inspection time and enables predictive vs preventive or condition-based or reactive maintenance. The paper aims at promoting the adoption of advanced DT architectures as part of the integrated fleet maintenance system. Accurate and real-time failure predictions, diagnostics, and optimized maintenance scheduling enabled by the DT is thought to significantly enhance aircraft's safety of operations, as well as ensure life-cycle cost savings for the current and future aircraft programs.

Keywords: aircraft landing gear, digital twin, operational data analysis, predictive maintenance

1. Introduction

The drag-brace subsystem of an aircraft stabilizes the landing gear (LG) during ground operations, and usually undergoes iterative redesigns to address cracking from metal fatigue over decades of service. Specifically, over the past two decades, the drag-brace design of the F-16 LG has undergone modifications in response to critical incidents and accidents [1, 2]. These modifications include transitioning from hydraulic to spring-based actuation systems, addressing such issues as collapses due to worn bushings (cylindrical linings to limit the size of the opening and resist wear), failures involving toggle and link vibration, and collapses due to overstress of the link subject to the resonance effects.

Substantial engineering research efforts have been dedicated to uncovering this phenomenon' root causes. However, despite accumulating big volume of data and experience, identifying the predominant factors affecting fatigue rates in the drag brace of F-16 LG remains a challenge. As a result, safe operations of this aircraft rely on scheduled LG disassembling (since the direct wear measurements are not even possible) and bushing replacement (Figure 1). Most of the time this happens prematurely.

Indeed, the condition-based maintenance where actions are taken based on monitored asset condition, would be a step forward compared to reactive maintenance, where actions are only taken when an asset fails, or preventive maintenance based on scheduled activities, but it takes a lot of resources. Prescriptive maintenance where optimized decisions are made based on predictions and predictive maintenance where models are used to predict the future asset failures are considered to be even a

better option [3]. Specifically, predictive maintenance promises cost savings over routine or time-based preventive maintenance because tasks are performed only when warranted.

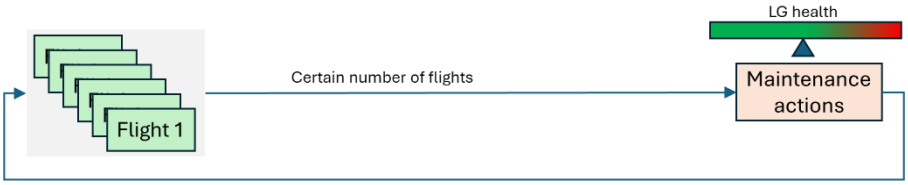

Figure 1 – Current schedule-based LG maintenance routine.

Digital twin (DT) technology promulgated by the U.S. DoD [4] creates a virtual representation of physical assets and has already proved to have a great potential for a variety of applications. Integrating a DT will enable shifts to more proactive maintenance strategies by providing real-time asset monitoring capabilities and the ability to run simulations to predict future failures and optimize maintenance decisions. Specifically, DTs can facilitate the condition-based processes with integrated sensor data, predictive strategies with integrated prognostic models, and prescriptive methods by linking predictions to the optimized maintenance plans. Hence, DTs provide key capabilities to transition maintenance programs to more intelligent and proactive approaches.

This research promotes exploiting a DT of LG to enable accurate and real-time failure predictions and diagnostics of drag-brace system of F-16 to fully eliminate, or significantly reduce costly and lengthy inspections affecting aircraft availability. To this end, Figure 2 shows the envisioned predictive LG maintenance routine relying on the combination of the physics-based and data-driven models providing insights, predictions, and supporting informed decisions.

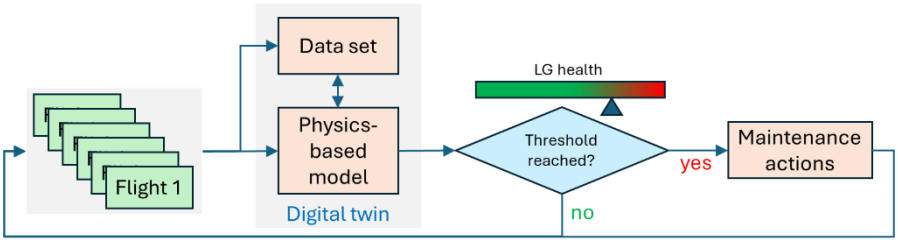

Figure 2 – Proposed predictive LG maintenance routine.

Developing an accurate DT of this system enables batch simulations that could help with predicting the wear rates in joints (bushings) depending on the actual loads on components during the high-stress landing phase in variable conditions. These predictions of the transition from a healthy state to a failure is the core in enabling proactive maintenance scheduling as shown in Figure 2. Overall, implementing predictive maintenance for a LG through DT technology offers such advantages as increased safety (reducing the likelihood of accidents), enhanced operational efficiency (minimizing unplanned downtime), cost effectiveness (lowering the costs of spare parts and labour and extending the overall lifespan of the LG components), and optimal resource utilization (optimizing manpower and material usage) [5].

While DTs promise to enable remote diagnostics and maintenance in the aerospace industry, significant barriers preventing their widespread adoption and implementation still exist. A primary challenge is the high development costs associated with building and validating a DT model. Constructing an accurate physics-based model requires extensive simplifications and assumptions, which may only partially replicate a true behaviour of physical system [6]. Validating the model is also time-intensive, requiring testing across a range of operating states and potential failure scenarios. For organizations with the limited budgets or compressed development timelines, these costs may seem prohibitive [7].

The lack of standardized processes for DT requirements definition, development, and implementation presents difficulties as well. With no repeatable framework to follow, organizations face steep learning

curves and struggle to scope DT functionality appropriately. This leads to functionality risks where the DT may not provide utility aligned to the stakeholder needs.

Finally, quantifying return on investment (RoI) for DT adoption remains a challenge. There are limited documented examples of DTs being successfully integrated into fielding strategies [4]. For large-scale programs like the F-35, with numerous fielded assets, positive RoI may be achievable. However, for smaller organizations with fewer deployed systems, the value is harder to predict. Without clear proof points, risk-averse sponsors may be dissuaded from investing in DT initiatives, especially for accelerated acquisition programs.

The primary objective of this research is to explore the concept of DT and its application within the engineering domain of the Air Force. This research investigates the factors influencing the LG wear during landings and ground operations exploiting DT technology. Ultimately, the research aims to facilitate the consistent integration and utilization of this technology within the operational framework of the F-16 fleet. Looking forward, this research serves as an initial step in the broader adoption of DT technology across various systems within F-16 and other aircraft.

The remainder of the paper is organised as follows. Section 2 provides a detailed description of F-16 LG system. Section 3 introduces the overall framework of DT of this system, followed by Sections 4-10, providing details on each component of the developed DT (these sections use some notional data on a typical F-16 aircraft.) Section 11 presents a procedure for DT tuning to keep it aligned with the existing and incoming streams of landing data. Section 12 illustrates an example of using the developed DT. The paper ends with conclusion.

2. Description of F-16 LG

This section describes main components of the F-16 LG system, and the drag-brace subsystem, in particular, and then lists the main factors influencing a bushings wear.

2.1 Drag Brace System

Figure 3a shows the main LG system obviously being one of the most critical components of aircraft, providing support and stability during take-offs, landings, and ground operations. The LG must bear the impact forces during these processes to relieve the strain on the aircraft's fuselage and therefore minimize potential damage. The LG design is crucial to support the high loads experienced during aircraft operations. At the same time, one of the significant factors to consider in aircraft design is the weight limit (a typical LG should account for not more than 3% to 6% percent of the maximum aircraft take-off weight [8]).

a) 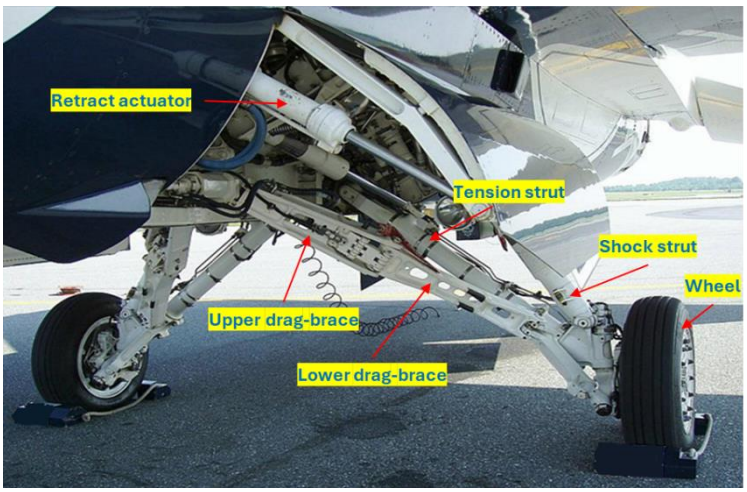

b) 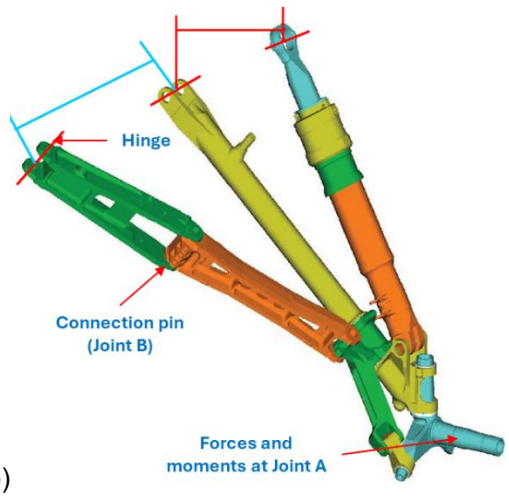

Figure 3 – Main LG components (a) [9] and CAD model (b) [10].

As shown in Figure 3a, the F-16 LG system encompasses various essential components, including the retractable mechanism, shock absorbers, wheels, brakes, and tires. These multiple components work to ensure the safe and efficient operation of aircraft's landing system. Figure 3b show the computer-aided design (CAD) model of the main LG.

The folding drag brace comprises an upper and lower parts connected by a shaft and bushings (Figure 4a). Within this joint, there are two types of bushings. The first type is the bushing located between the lower brace and the shaft (referred to as 'bushing lower'). The second bushing type is located between the upper brace and the shaft (referred to as 'bushing upper' and denoted as C1 in Fig 4b). In this joint, there are six bushing sleeves: four "bushing upper" and two "bushing lower". This research aims to predict the level of wear in all bushings.

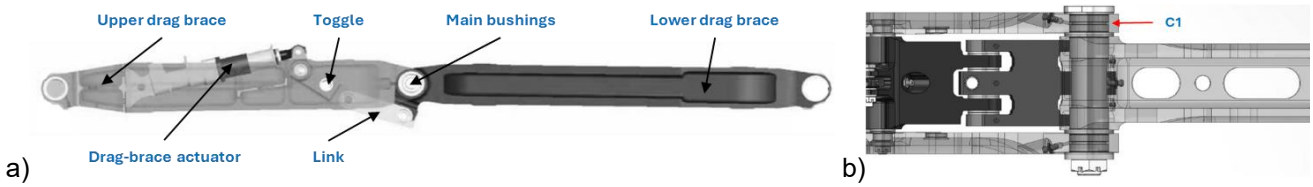

Figure 4 – Drag-brace assembly (a), and Joint B (b).

The upper and lower parts are also connected with the drag-brace mechanism (see Figure 4a). This mechanism (also called down-lock) is a critical part of the LG system that ensures the proper locking and stabilization of the gear during ground operations. The downlock mechanism consists of link assembly, toggle assembly, and actuator. The mechanism holds the drag brace in the centre with the actuator spring. The link assembly is a one-piece forging that provides a link between the fixed lugs of the lower drag brace and the clevis of the upper toggle assembly. The toggle assembly is a one-piece forging mounted to the upper drag brace. The upper end of the upper toggle link assembly is connected to the actuator rod end and the lower end is connected to the lower toggle link assembly. The actuators are attached to the upper drag braces with their rod ends connecting to the main gear toggle assemblies. As the gears lower, the actuators extend to mechanically lock the drag braces. The actuators have springs supplying the actuator extending force, hence, hydraulic pressure is not required for downlocking. Hydraulic pressure is normally supplied to the actuator extend ports to minimize reservoir exchange volume and to block the actuator internal cavities from entry of contaminating or corrosion producing substances, the actuator is internally constructed so that no downlocking forces is produced by hydraulic pressure. The springs-loaded feature of the actuators provides the means of maintaining the position of their respective drag braces on centre unless hydraulically retracted. This mechanism prevents the gear from retracting unexpectedly and maintains structural integrity during taxing, take-off, and landing.

During operations, LG experiences various frictional forces including the so-called journal friction force and seal friction force. The journal friction force arises from the normal force acting in the joints and bushings, while the seal friction force results from the friction of internal seals within the shock absorber, and depends on the internal gas pressure. Due to their significant impact on LG behaviour, these frictional forces must be considered in dynamic modelling to ensure the fidelity of the model and its ability to represent a physical system.

2.2 Factors Affecting Structural Health of Drag Brace

During different phases of aircraft operation, LG is subject to the following loads:

- Vertical loads occurring during take-offs and landings when the aircraft's weight is transferred to the LG through the wheels;
- Lateral loads resulting from the side forces during crosswind landings or taxiing; and
- Horizontal loads caused by take-off and landing roll acceleration (thrusting) and deceleration, (braking).

Specifically, during landing, the main load cases for the main LG are spin-up and spring-back. These loads are significant during landings since the impact of aircraft on the ground causes a sudden increase in forces acting on LG components. Spin-up refers to the initial contact between the aircraft wheels and a runway during touchdown. The LG experiences a significant load due to the rapid acceleration of the wheels as they transition from a static state to matching the aircraft's ground speed. This load results from the inertia of LG components and sudden increase in rotational speed.

After absorbing the impact forces during landing, the LG components undergo deformation. The LG rebounds and returns to its original position, releasing the stored energy. This (spring-back) action can result in an additional load on the LG system, impacting its structural integrity and damping characteristics.

3. LG DT Architecture

Figure 5 represents the overall architecture of the envisioned hybrid physics-informed and data-driven DT of the main LG taking advantage of data fusion [11].

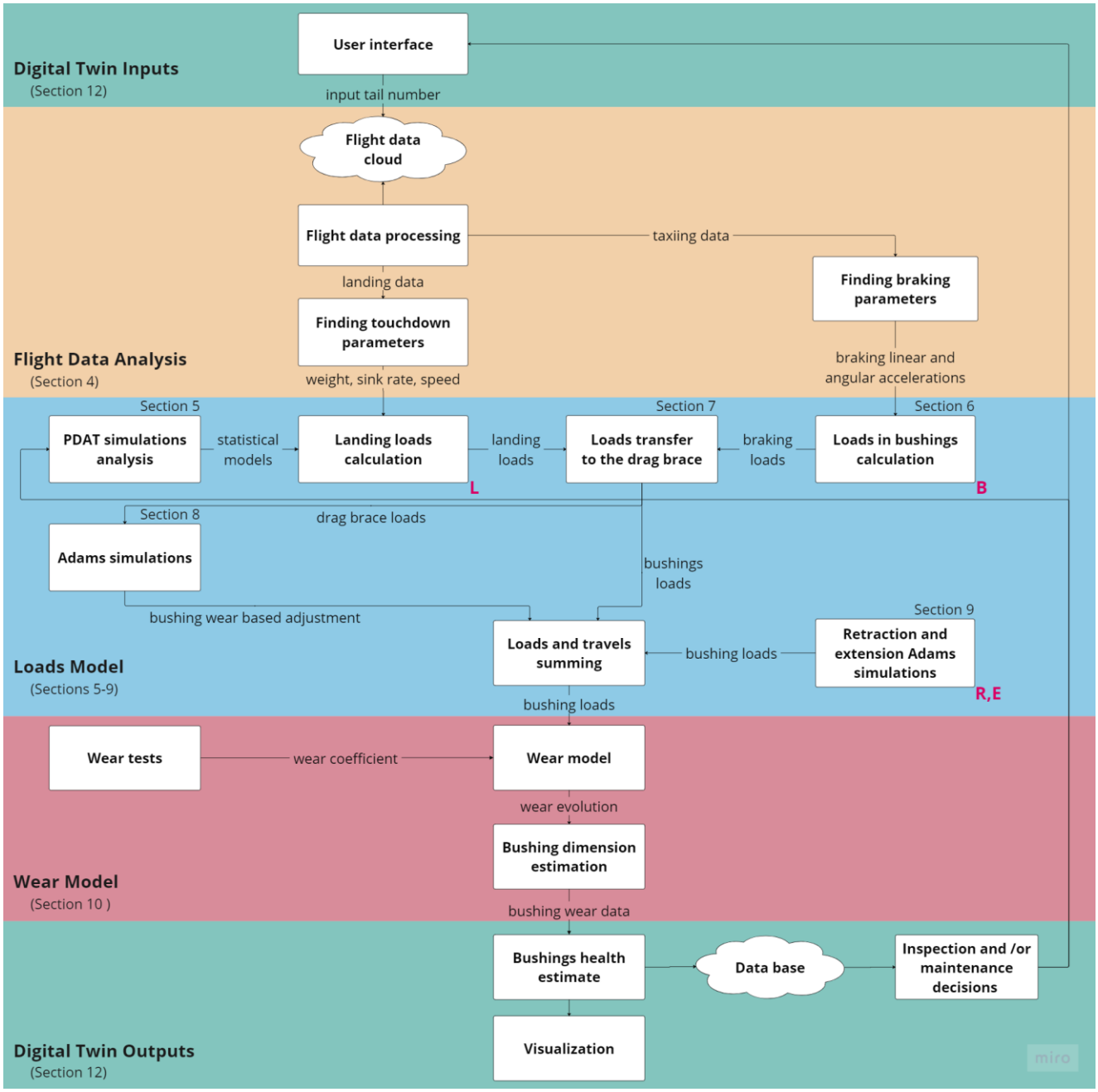

Figure 5 – DT data flow.

This DT is composed of the following blocks that are described in more details in the following sections:

- Flight Data Analysis block (to be discussed in Section 4) analysing raw flight data provided from the repository to identify touchdown and taxiing brake events and recovering several key parameters at these time instances;

- Loads Model block calculating the loads caused by landing (Section 5) and braking (Section 6), transferring them from the tires to the LG joints (Section 7), adding the (nonlinear) effect of the bushing wear (Section 8) and loads caused by LG opening and folding (Section 9);
- Wear block (Section 10) analysing stresses in bushings and converting them to the volume of the total wear for Joint B bushings.

As a result of implementing this proposed DT, the dimensions of the main bushings are calculated for all scheduled flights and all aircraft in a squadron, followed by computing the number of remaining sorties for the bushings to reach the maintenance threshold – maximum wear limit (MWL) – indicating the need to replace them. These data are conveniently presented using the DT's dashboard.

4. Flight Data Analysis

This section provides details on processing the real flight data to determine a set of critical parameters pertained to touchdown and braking events.

4.1. Flight-Data Recording in Preprocessing

The analysis is based on flight data recorded by onboard sensors. For the purpose of DT development, these recorded data undergo several preprocessing steps. First, raw data are cleaned and structured meaning that all irrelevant information is removed. Then, remaining data are transformed into a usable format. Second, the selected raw data are georeferenced and visualized for pattern and anomaly identification. This involves identifying different relevant stages of landing including touchdown, roll out, braking, and taxiing. Various critical parameters for further analyses include the sink rate, ground impact speed, angle of attack, pitch and roll angles, and ground distances. These parameters are then used to derive vertical and horizontal accelerations, distances, and more.

For this research effort, flight data came in two different formats: Type A and Type B. Type A data includes physical parameters of an aircraft recorded at different rates. For example, the horizontal velocity vector components, V_x and V_y, are recorded at the 2*Hz* rate, while other parameters (angle of attack α, sink rate V_z, output of a Weight on Wheel (WoW) sensor, and pitch angle θ) are recorded at the 8*Hz* rate. Type B data includes such parameters as aircraft weight, acceleration along the z axis, and aircraft altitude. These parameters are recorded at the sampling rate higher than that of Type A data and as such are more accurate for the purpose of finding the touchdown event (as opposed to a specially dedicated WoW sensor).

4.2. Localizing Touchdown Event

The touchdown event can roughly be determined by using the outputs of the WoW sensor, which switches from "Flight" (1) to "Ground" (0) at the perceived touchdown. However, this switch instance is usually delayed until the nose wheel touches the ground. By this moment, the sink rate and angle of attack are already zero for a few seconds. As a result, the aircraft altitude and vertical acceleration serve as much more accurate indicators. The developed algorithm starts searching for a spike in vertical acceleration when the aircraft descends below 10ft. Figure 6 shows an example of touchdown event identification using this approach.

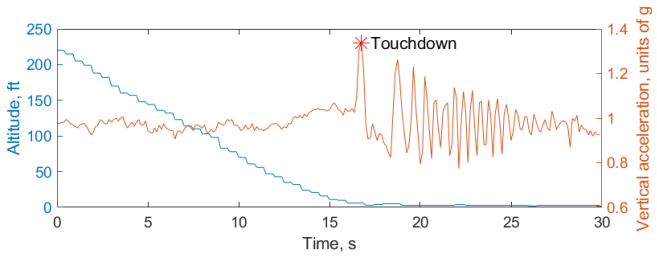

Figure 6 – Time history of aircraft's height (left y-axis) and vertical acceleration (right *y*-axis).

4.3. Assessing Touchdown Parameters

Calculation of landing parameters is based on the identified touchdown event. Since the touchdown time instance (based on Type B data) usually falls between the two intervals of Type A data, linear

interpolation is utilized to estimate these parameters. Figure 7a visualises a WoW sensor output adjacent to the identified touchdown event (clearly showing that the identified touchdown event marked by a vertical yellow line occurs a couple of seconds sooner compared to the WoW "Ground" signal). Figures 7b, 7c and 7d show the corresponding time histories of aircraft speed, sink rate, and angle of attack, respectively. The specific values of these states (plus aircraft's weight) at touchdown serve as the inputs for the following steps of the bushing wear analysis (see Figure 5).

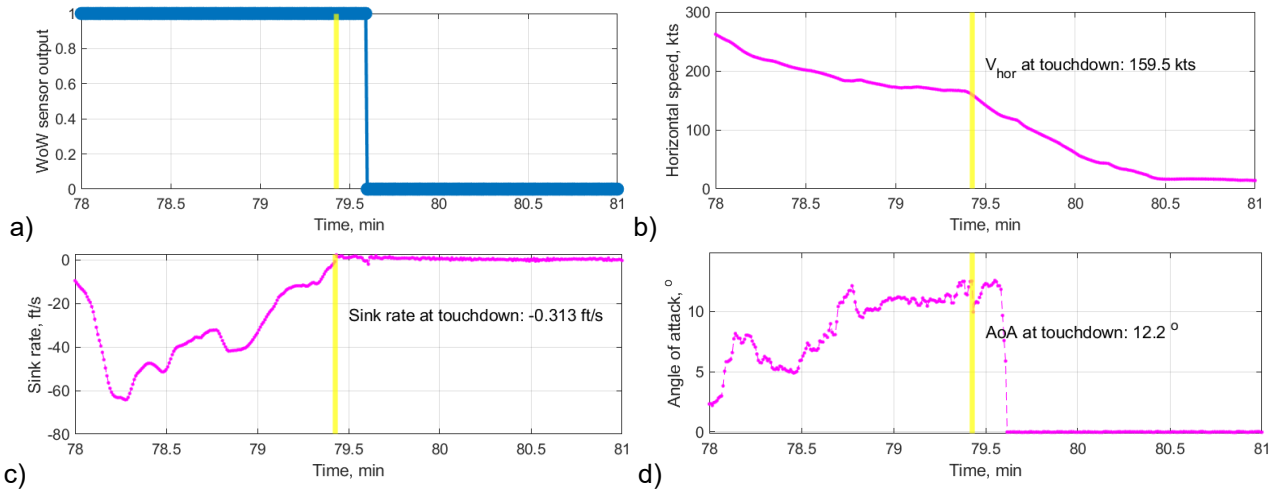

Figure 7 – Time histories of the WoW sensor output (a), speed (a), sink rate (c), and angle of attack (d).

4.4. Braking Data Analysis

Braking events during after-touchdown and before-take-off taxiing are identified using the ground speed profile (Figures 8a and 8b). First, it is filtered using a moving average filter to eliminate measurement noise. Second, the aircraft's horizontal acceleration (the ground speed gradient) is computed and filtered yet again (Figures 8c and 8d). Then, the developed algorithm identifies the negative peaks – hard brake events with deceleration of more than $1 ft/s^{-2}$. These identified braking events are denoted in Figures 8c and 8d by a star marker.

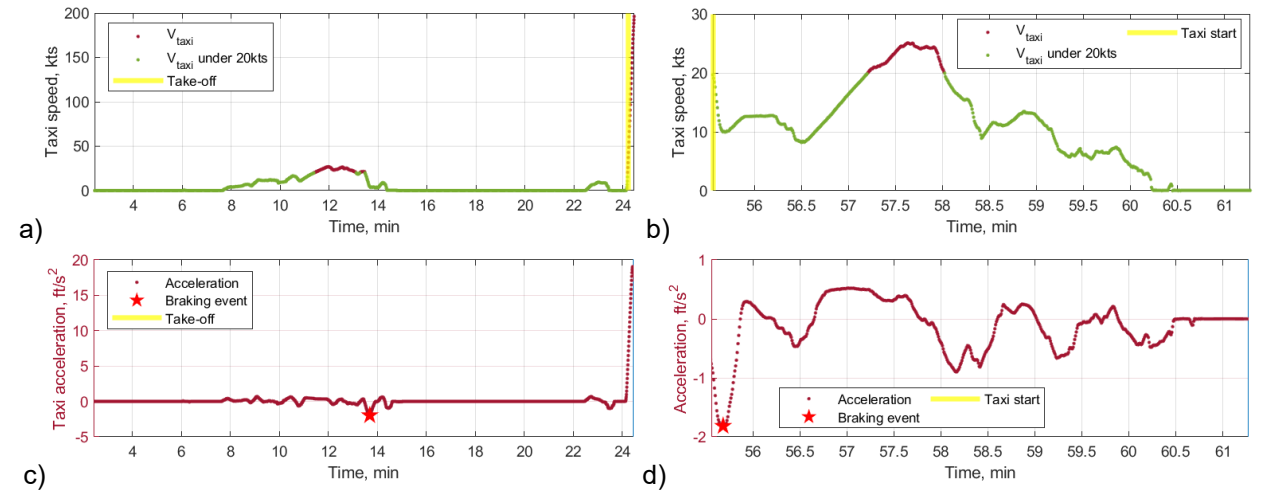

Figure 8 – Time histories for the taxi speed (a,b) and acceleration (c,d) before take-off (a,c) and after touchdown (b,d).

It should be noted that this significant deceleration threshold was also used to filter aerodynamic braking that has no effect on the LG loads. This is because in the case of aerodynamic braking the resulting force is applied near the centre of gravity (CG) and the change in pitch angle is negligible. On the contrary, when the brakes are used - the force is applied at the main tires bottom which causes a nose-down pitching moment (Figure 9).

The results of this analysis are stored as a list of time stamped braking events with the peak deceleration and corresponding pitch rate.

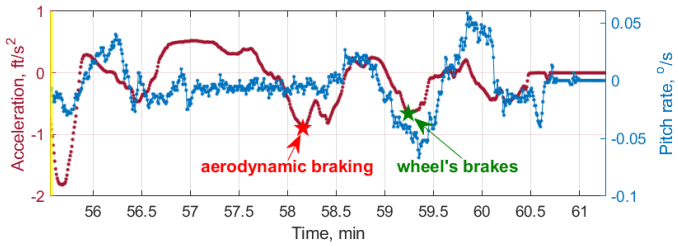

Figure 9 – Time history of taxiing acceleration (left y-axis) and change in pitch rate (right y-axis).

5. Calculating Landing Loads

This section describes how the envisioned DT of Figure 5 converts the identified touchdown and braking parameters to the corresponding main LG loads. This is done by using the proprietary dynamic analysis tool (PDAT).

5.1. Dynamic Analysis Tool

Clearly, the loads in the LG system are primarily defined by the following factors:

- Aircraft weight, influenced by such factors as the flight configuration and the remaining fuel;
- Sink rate directly affecting the loads in spin-up and spring-back conditions;
- Touchdown speed directly affecting the landing loads; and
- Flight configuration, which may involve asymmetries (not addressed in this study) and variations in CG location.

Unfortunately, the known mathematical models developed to accurately represent the LG's behaviour at touchdown were found not suitable for this research. First, since the F-16's LG involves an angular deviation relative to the ground (which is not a 90° angle as assumed by the existing models). This introduces additional complexity requiring a more sophisticated analysis. Second, the existing models do not account for critical environmental parameters such as the angle of attack, ground impact velocity, or aircraft's configuration. Third, these models do not address various energy losses, such as damping or joint friction.

That is why in lieu of developing a mathematical model, a PDAT was used. This tool aims to simulate complex behaviours observed during landing drawing from both the literature review and dynamic software to improve predictive accuracy and reliability of the LG loads. The inputs to this dynamic analysis tool are the aircraft weight, sink rate, and touchdown speed.

The design of experiments was utilised in this study to query PDAT with a variety of realistic inputs to cover the landing weight withing the allowance weight range, sink rate corresponding to soft (1-2*ft*/*s*), medium (3-4*ft*/*s*), and hard (5-6*ft*/*s*) landings, and touchdown speed within the [143;162]*kts* range (while maintaining a constant angle of attack at 13°).

5.2. Vertical and Horizontal Loads

The results of PDAT simulations are shown in Figure 10a (for the notional vertical load on tires) and Figure 10c (for the notional horizontal / drag load). (The drag load is considered positive when the load is in the direction opposite to the aircraft's movement.) Time histories are limited to the first five seconds following the touchdown and filtered to eliminate noise from the damper and spring reaction.

As seen from Figure 10c, during the first 5 seconds following the touchdown, the horizontal load experiences 12 peaks, after which it stabilizes. The developed algorithm allows to automatically find these events and subdivide the entire time range onto 12 (uneven) segments, shown in Figure 10d. Each segment has a maximum or minimum peak depending on landing parameters. The horizontal load is negative until Segment 3, which occurs 0.25*s* after touchdown. This negative load indicates the beginning of the LG spring-back phase. A similar approach is applied to a vertical load plot (Figure 10b) as well.

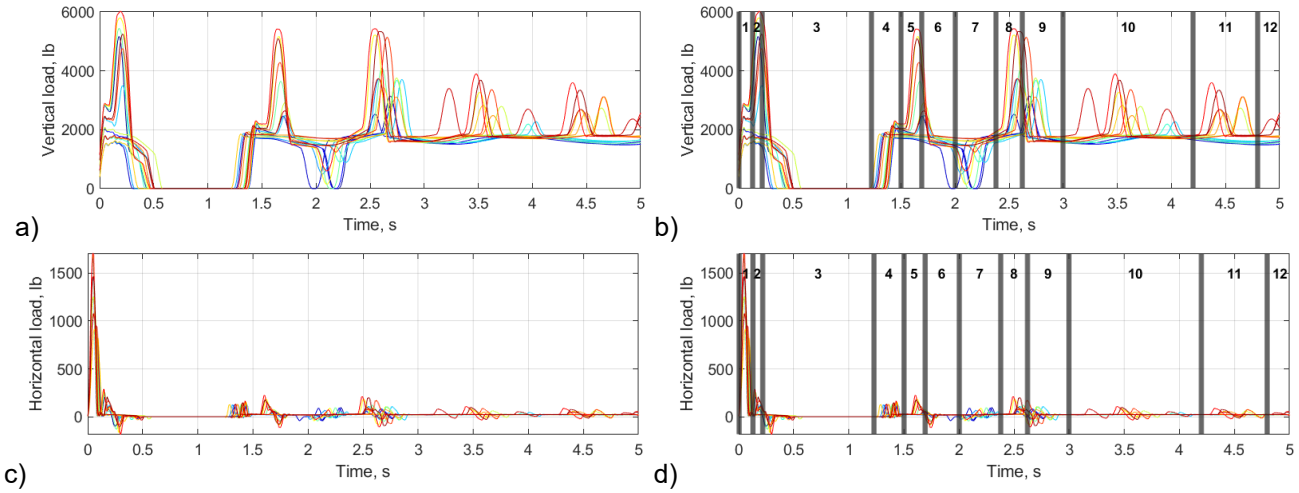

Figure 10 – The vertical (a, c) and horizontal (b, d) loads following touchdown.

Machine learning was first thought as a tool predict the load response. However, since this response in not linear, it would require running hundreds of simulations. Hence, this study pursued an alternative approach. Rather than obtaining the landing load profile with precision, a simple tool was developed to predict just the key peak loads.

5.3. Predicting the Peak Loads

In each segment (like the ones shown in Figures 10b and 10d), the maximum (or minimum) load was first calculated. Then, a stair-step graph was created to approximate a simplified vertical and horizontal loads.

To illustrate this approach, consider Figure 11. From the analysis of the central peaks of the horizontal force, the average response time of each peak was estimated to be around 0.15*s.* Subsequently, for each segment, a linear regression analysis involving two variables (normalised aircraft weight and sink rate) was executed. (Linear regression served as a sufficient quasi-optimal solution identifying the relationship between the variables (weight, sink rate) and the peak height.) As seen from Figure 10d the horizontal load peaks do not necessarily occur in every segment of the simulation. The peaks exhibiting the load of less than 200lb, were considered negligible and ignored. Figure 11 shows the resulting stair-step approximation. The average *p*-value for the horizontal load regressions was 7.7×10^{-5}, and the average *R* squared adjusted value was 0.88.

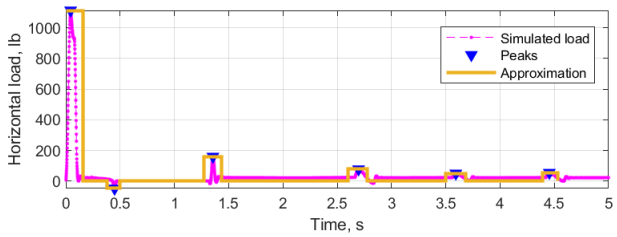

Figure 11 – Horizontal landing load stair-step approximation.

Similar to horizontal force, linear regression was also performed for each segment of the vertical load (Figure 10b). The average *p*-value for the vertical load regressions happened to be 4.5×10^{-5}, and the average *R* squared adjusted value was 0.87.

Utilising the created regressions, stair-step dynamics could be created for any combination of the input parameters. For example, assuming the maximum landing weight and sink rate, the vertical and horizontal load landing profiles would look like what is shown in Figures 12a and 12b, respectively.

6. Braking Dynamics

Stepping on the brakes during taxiing and after-touchdown roll out creates the additional loads on the drag brace. In fact, the drag brace is designed as a crucial element to help to structurally sustain

braking. The calculation of the braking loads is based on the acceleration estimates as was shown in Figure 9. During sharp braking, the rolling-friction coefficient on the main LG μ_f, which is on the order of 0.02-0.04 for paved runways, switches to the braking coefficient μ_b, of the order of 0.4-0.6 (for the dry runway) or 0.2-0.3 for the wet runway [12], i.e. sharply increases 15-20 times. The entire horizontal acceleration is then to be handled by the main LG (Figure 13).

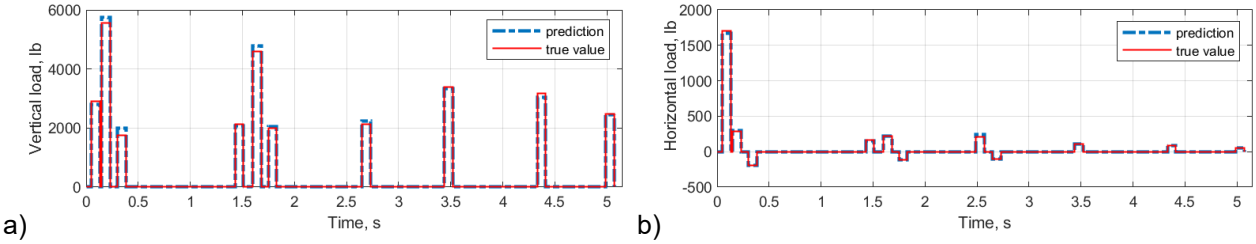

a) b)

Figure 12 – Prediction of the vertical (a) and horizontal (b) landing loads for a specific landing configuration.

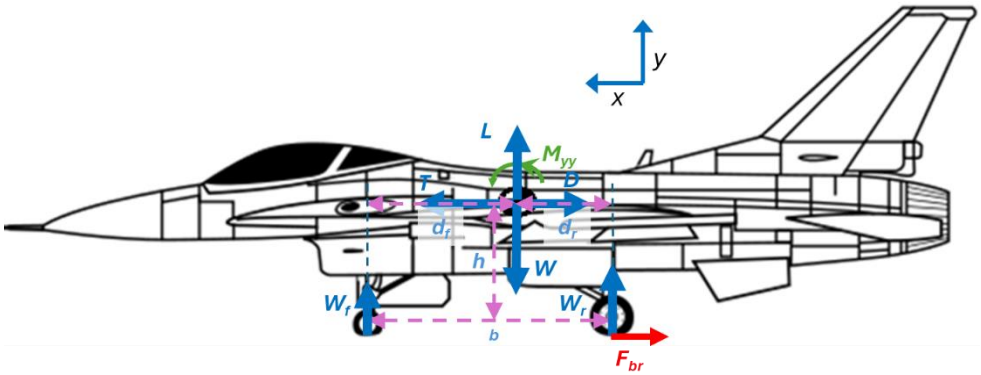

Figure 13 – Loads on landing gears while braking.

The horizontal load on each main tire is then

$$F_{br} = 0.5Wag^{-1} \tag{1}$$

where W is a total aircraft weight, g is the acceleration due to gravity, and the acceleration a comes from the flight data analysis (Figure 9).

The vertical load on the main LG during braking is not explicitly measured but can be estimated from the following two equations:

$$W = L + W_f + W_r \tag{2}$$

$$W_f\, d_f - W_r\, d_r - 2F_{br}h = I_{yy}\ddot{\theta} \tag{3}$$

where I_{yy} is the moment of inertia.

Combining (2) and (3), assuming $W \gg L$, and accounting for $b = d_f + d_r$, we arrive at

$$W_f = \left(Wd_r + Wahg^{-1} + I_{yy}\ddot{\theta}\right)b^{-1} \tag{4}$$

$$W_r = 0.5\left(Wd_f - Wahg^{-1} - I_{yy}\ddot{\theta}\right)b^{-1} \tag{5}$$

In (4) and (5), the angular acceleration $\ddot{\theta}$ also comes from the flight data analysis (Figure 9).

7. Loads Transfer

The next modelling block (see Figure 5) transfers the landing and braking loads calculated at the tire's bottom to the relevant bushings in the drag-brace assembly (see a simplified representation in Figure 3b). This requires a knowledge of specific LG geometry and operations.

First, the ground loads are transferred to Joint A (tire axis)

$$P_A = \begin{bmatrix} F_{x_A} \\ F_{z_A} \\ M_{z_B} \end{bmatrix} = \begin{bmatrix} F_{br} \\ W_{dr} \\ -rF_{br} \end{bmatrix} \tag{6}$$

where P_A is the load vector in Joint A, r is the tire rolling radius, F and M are the forces and moments in the relevant axes. Then, the loads in Joint A are transferred to Joint B (lower drag brace)

$$P_B = \begin{bmatrix} F_{x_B} \\ M_{z_B} \end{bmatrix} = R_A^B P_A \tag{7}$$

where P_B is the load vector in Joint B, and R_A^B is the transfer matrix from Joint A to Joint B. This matrix varies depending on the situation. It changes during braking or landing due to LG geometry. Even during landing, there are differences in this transfer matrix: during spin-up (when aircraft is in the air), the matrix is "free knee", when spring-back occurs at touchdown, it is "fixed knee". Using the moment equations on the knee joint, certain parameters can be calculated as follows:

$$M_{z_{knee}} = F_{x_B}\Delta y + \mu_1 M_{z_B} \tag{8}$$

$$|M_y| = |F_{x_B}|\Delta z \tag{9}$$

$$P_{link} = \mu_2 M_y \tag{10}$$

In (8)-(10), Δy and Δz are deflections in Joint B during braking, P_{link} is the tension force in the main pin, M_{zknee} and M_y are the moments in the main pin, μ_1 and μ_2 are specific linear parameters.

Finally, using the moment equation for the pin, the forces on the four bushings in Joint B can be found via

$$R_1 = \gamma(-F_{x_B} + \mu_3 M_{z_{knee}} + P_{link}\cos(\beta)) \tag{11}$$

$$R_2 = \gamma(-F_{x_B} + \mu_4 M_{z_{knee}} + P_{link}\cos(\beta)) \tag{12}$$

$$R_3 = \gamma(-F_{x_B} - \mu_4 M_{z_{knee}} + P_{link}\cos(\beta)) \tag{13}$$

$$R_4 = \gamma(-F_{x_B} - \mu_3 M_{z_{knee}} + P_{link}\cos(\beta)) \tag{14}$$

where γ, μ_3, μ_4, and β are specific linear and angular parameters of the main LG brake-brace assembly.

8. Relative Displacement of Parts in Brake-Brace Assembly

One of the factors influencing wear, beyond the forces previously modelled, is the magnitude of displacement (travel) when a certain force is applied to a multi-part drag brace [13]. The forces and moments acting on the drag brace generate a dynamic response within the LG system which involves a rotational movement of the upper brace with respect to the lower brace. As a result, the wear rate is not constant throughout the life of bushings, but rather increases as more "freedom" is created between the pin and bushings of the drag brace. This phenomenon was explored taking the tension (or compression) force P_a, and the moment M_z and exploiting the dynamic LG model developed using multibody dynamics software Adams.

The required simulations assumed a wheels-down LG position with the drag brace opened (fully expanded) and locked. Four cases were executed as follows:

1) The "ideal" case, where the holes axes in the upper and lower locks are axially symmetrical, and therefore there is no contact between the braces;
2) The minimum tolerance case, assuming no wear at all (the initial size of bushings of 1.1192");
3) The maximum tolerance case with the initial size of bushings of 1.1204"; and
4) MWL case with the initial size of bushings of 1.1224".

For each of these four cases, seven different landing and take-off scenarios featuring different combinations of force P_a and moment M_z were executed. Figure 14 shows an example of how the angle between the upper and lower drag braces (see Figures 3b and 4a) changes as a function of time. Comparing Figure 14a (Case 1) with Figure 14b (Case 4), the difference in amplitude profile and frequency can be observed. The larger the inner diameter of bushings, the greater the rotational distance (travel). This non-linear dependence was incorporated in the model.

9. Retraction-Extension Loads

The LG retraction and extension process during the initial climb and final approach causes the main bushing of the drag-brace assembly wear as well. The retraction process of LG begins with the angle between the upper and lower braces being 179° (fully open and locked) (Figure 15a) and ends in 5

seconds with both braces at an angle of 13.5° relative to each other (Figure 15b) [14]. While retraction-extension, a load is applied to LG joints from the retract actuator or the weight of the gear. These loads are also influenced by the airspeed and cross winds.

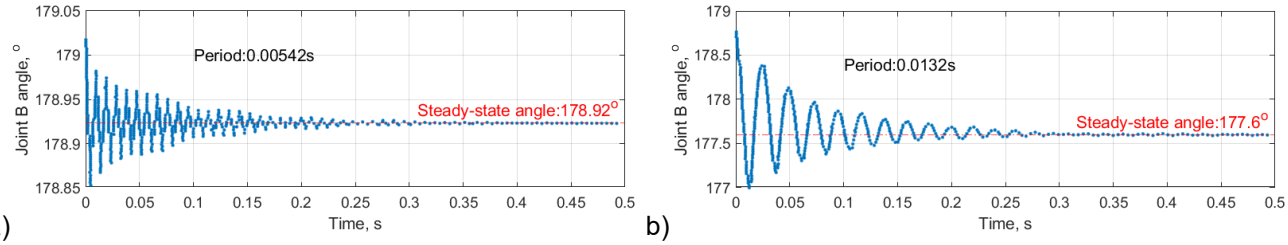

a) b)

Figure 14 – Simulation response for the ideal (a) and MWL (b) cases for one of braking scenarios.

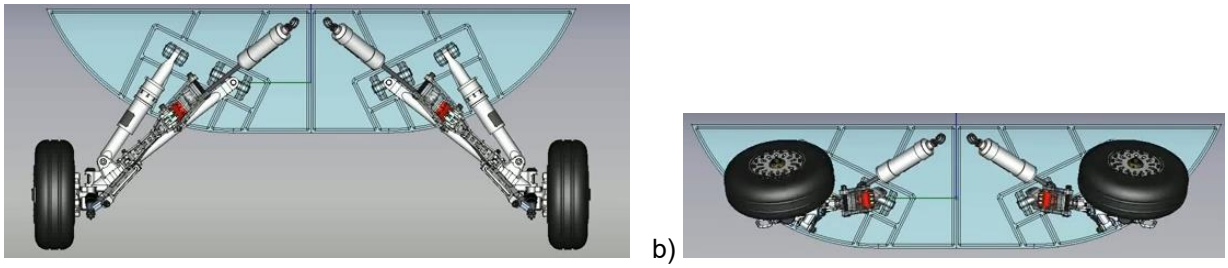

a) b)

Figure 15 – Main LG in the fully extended (a) and retracted (b) positions [14].

These loads were estimated and modelled in the developed DT using the same Adams software discussed in the previous section. Unlike multiple cases and scenarios explored in the previous section, a worst-case scenario, independent of airspeed and crosswinds, was analysed and implemented in the DT. To this end, the section area of the retract actuator for compression loading was calculated as

$$A_c = \frac{\pi}{4}\left(D_{cylinder}^2 - D_{sleeve}^2\right) \tag{15}$$

and the area for tension loading as

$$A_t = \frac{\pi}{4}\left(D_{cylinder}^2 - D_{piston}^2\right) \tag{16}$$

Hence, the retraction and extension forces were calculated by multiplying the corresponding areas by the constant (3,000 psi) hydraulic pressure

$$F_{retraction} = A_c P_{hydraulic} \approx 12\ klb \tag{17}$$

and

$$F_{extension} = A_t P_{hydraulic} \approx 9.6\ klb \tag{18}$$

As the LG door reaches the fully open position, the lock releases the lock roller on the shock strut allowing the LG to free-fall to the extended position. The retract actuator is connected to the hydraulic system return on both piston sides during extension. Figures 16a and 16b show the results of the Adams simulation which were incorporated into DT. As seen from these figures, the dynamic force obtained after running the simulation was composed of a variable force profile with multiple peaks throughout the retraction and extension processes. The average load of the peaks in the retraction process is 1.97*klb*, while the average load of the peaks in the extension process is 8.36*klb*.

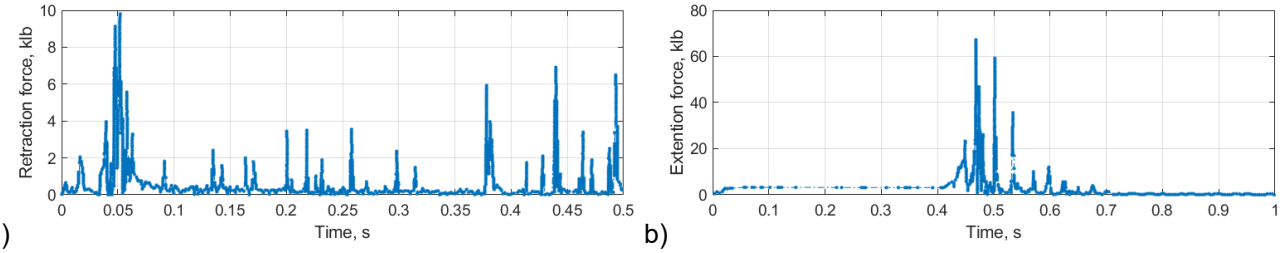

a) b)

Figure 16 – Dynamic forces in the main bushings during retraction (a) and extension (b).

10. Evaluating Bushing Wear

After developing the dynamic model based on theoretical insights gained through the literature review, this section focuses on a wear modelling. The aim is to accurately analyse and predict the wear rates in LG bushings.

10.1 Mechanisms of Wear

Wear is the gradual damage and removal of material from a surface due to relative motion and contact pressure between two surfaces. In bushings, wear typically occurs due to the repetitive sliding or rolling contact between the bushing and a mating component, such as a shaft. There are four main mechanisms that contribute to the wear resistance of bulk materials [15]:

- Adhesive wear occurring when microscopic particles from one surface adhere to another due to high contact pressure and friction. As the surfaces continue to slide or roll, these particles are torn away, resulting in material loss;
- Abrasive wear caused by hard particles, such as dust or debris, between the mating surfaces. This results from hard, foreign particles (e.g., grit) between the mating surfaces (these particles act like abrasives, causing abrasion and wear on both surfaces);
- Fatigue wear arising from surface fatigue caused by cyclic loading. As cyclic loading continues, cracks form on or beneath the surface, propagating and generating wear particles; and
- Corrosive wear (the least common of the four main wear mechanisms) is uniquely influenced by environmental factors depending on the material of two parts.

The main form of wear studied in this research was fatigue wear. The bushing experiences high loads and cycles due to ground loads and the movement of the two parts it connects. These loads and cycles result in significant wear on bushings leading to excessive clearance. This can inadvertently cause the LG to fold during landing, potentially resulting in a catastrophic accident. To reduce fatigue wear, a lubrication material is used between the parts. This lubrication material helps to reduce friction and heat generation, which can contribute to fatigue wear.

10.2 Methods for Wear Prediction and Key Factors in Wear Modelling

Accurately predicting wear progression in bushings is critical for estimating service life and enabling condition-based maintenance. However, the complex nonlinear nature of wear processes poses challenges for developing robust predictive models. Several significant techniques have been applied to model and forecast bushing wear rates

- Analytical models based on the Archard's equation and other models relating radial wear to pressure, sliding distance, and material properties;
- Finite element analysis simulating contact stresses and incremental wear depth using computational models; and
- Empirical models fitting wear data to analytical expressions related to operating factors and used to extrapolate the wear rates to new conditions.

The evolution of wear is affected by various parameters [16]. The main factors that affect wear are

- Contact pressure, the force per unit area at the interface of two contacting surfaces (higher contact pressures can intensify wear because they increase the material deformation and adhesion between two surfaces);
- Sliding speed, the relative speed at which two surfaces move to each other (higher sliding speeds can increase wear rates because faster motion can result in more frequent and forceful surface interactions);
- Temperature, so that elevated temperatures can promote adhesive wear by softening materials and increasing their propensity to adhere and transfer material from one surface to another. On the other hand, high temperatures can also enhance the effectiveness of specific lubricants in reducing friction and wear;
- Material properties, such as hardness, surface roughness, and coating (softer materials tend to wear more quickly when in contact with harder materials);
- Lubricant, creating a protective barrier between surfaces, minimizing direct contact and reducing friction; and

- Environment, such as humidity, chemical exposure, and the presence of abrasive particles, that can influence wear (for example, high humidity can exacerbate corrosion-related wear [17]).

10.3 Modelling Bushings Wear

Bushings are made of C63000 Nickel Aluminum Bronze (AMS 4640). The material is a type of wrought aluminum bronze that is forged or extruded and contains nickel, which makes it exceptionally strong and tough. It is used in applications that require higher mechanical properties, such as in equipment for the energy industry, aircraft, marine, and various other industrial applications.

Since bushings and bearings are mechanical components that are subject to high pressures and friction during their operation, lubricants are employed to improve the performance and extend the lifespan of these components. Using lubricants not only ensures smoother motion but also reduces wear and friction, thereby reducing maintenance costs. It is important to note that the choice of lubricant is critical and must be based on various factors such as operating conditions, temperature, and load. Therefore, proper selection and application of lubricants are essential to ensure optimal performance and longevity of bushings and bearings.

In the F-16 drag brace, the main bushings are filled with based-oil grease, MIL-PRF-81322G. It features a synthetic base oil and an organo-clay thickener, its NLG I 1.5, offering excellent oxidation stability, low-temperature fluidity, and high-temperature performance. This grease meets stringent military and aviation specifications, making it ideal for use in aircraft landing gear, helicopter rotor heads, and other critical components.

The literature review reveals that the 1953 Archard's model [18], an equation that estimates the wear rate in sliding contacts, has been previously employed in other research studies to measure wear in bushings

$$w = kPs = kPVt \tag{19}$$

In this formula, w is the radial wear, k is the coefficient of wear (CoW), P is the contact pressure, and s is the sliding distance, which can be replaced by Vt, a product of a sliding velocity and time. Although the model assumes a constant sliding velocity, some researchers explored non-constant velocities as well [19]. The amount of wear is directly proportional to the product of P and V, material properties, and time.

10.4 Contact Stress of Pin – Loaded Lug

Consider a pin of diameter D_p in a bushing of length L supporting a stationary radial load F (Figure 17). This model accounts the pin-hole clearance and considers the actual contact force transfer between the pin and the lugs. This approach leads to the formula for determining the maximum contact pressure on the contact surfaces in the pin-loaded lug. The maximum pressure distribution value on the bushings can be determined as [19]

$$P_{max} = \sqrt{\frac{FE_e}{\pi L D_e}} \tag{20}$$

where D_e and E_e are the equivalent Young's modulus and contacting diameter respectively calculated from

$$\frac{1}{D_e} = \frac{1}{D_h} - \frac{1}{D_p} \tag{21}$$

and

$$\frac{1}{E_e} = \frac{1-\nu_h^2}{E_h} + \frac{1-\nu_p^2}{E_p} \tag{22}$$

In (21)-(22), D_h and D_p are the diameters, υ_h and υ_p are the Poisson's ratios, and E_h and E_p are the Young's modulus of the pin and bushing respectively. Combining (19) and (20) yields

$$w = k\sqrt{\frac{FE_e}{\pi L D_e}}s \tag{23}$$

10.5 Experimental Determination of Coefficient of Wear

Since no information on the CoW of C63000 was found, a wear test to determine the CoW k with and without lubrication was conducted. The Nanovea T50, a standard modular tribometer, was used to

evaluate the tribological property. The ball-on-disk wear testing machine presses the stationary ball against the rotating disk (Figure 18). The tribometer measures the coefficient of friction (CoF), wear rate, temperature, and several other tribology parameters.

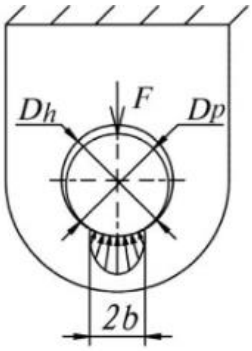

Figure 17 – Hertz pressure distribution on a boundary-lubricated bushing [19].

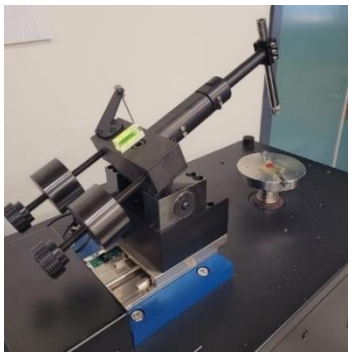

Figure 18 – Test sample is placed on the Nanovea T50.

In absence of C63000, the wear test was conducted on C63200. Both bronze alloys, C63000 and C63200, share 98% of their average composition and have highly similar mechanical properties [20]. Both materials are used in aviation and marine industries to resist wear in applications such as bearings, bushings, and shafts. Therefore, C63200 is used in the wear test to determine the bushing CoW.

The lubricant utilized in this test, Mobilgrease 28, is the polyalphaolefin clay-based multipurpose airframe and wheel bearing grease of choice for many aircraft operators around the world and possesses material properties identical to the grease employed in F-16 landing gear, USAF MIL-PRF-81322G [21]. For the first test, a C63200 metal sample measuring size 30*mm* x 25*mm* x 2*mm* was employed and covered with a thin layer of grease. The second test used the same sample, but without a layer of grease – which represented dry sliding conditions. The second test compared dry sliding and lubricated sliding to understand the role of grease in wear bushing and friction.

As mentioned already, the test was conducted using a ball-on-disk method. A stationary load of 5*N* was applied to the rotating disk with the sample. The material ball was made of stainless steel (ss304) according to the pin applied in the bushing. The radius of the ball was 1.5*mm*, the disk speed was 100 RPM, and the duration of each test was 60*min*, with a wear track diameter of 6*mm*.

The frictional properties were evaluated by recording the average CoF values obtained during the tests. The 3D non-contact type optical profilometer, NewView 7100, was used to analyse the depth and width of the wear tracks for an accurate quantification of wear. The wear volume loss or volume change after wear, ΔV, was calculated as [22, 23]

$$\Delta V = \frac{\pi r_t w_d^3}{6 r_b} \tag{22}$$

where r_t is the wear track radius, w_d is the wear track width, and r_b is the ball radius.

According to Archard's wear model, the wear volume with the applied normal load, P, and the sliding distance, s, was used to determine the specific wear rate or CoW, k

$$k = \frac{\Delta V}{Ps} \tag{23}$$

10.6 Wear Test Results

As expected, a significant contrast between CoF for the dry and grease tests was revealed (Figure 19). The reduction in friction for the grease test is obviously due to the lubricating properties of grease, which forms a thin layer between the two surfaces and helps minimizing the frictional force between them. As seen from Figure 19, the use of grease reduces friction by the factor of 3…5, which corroborates other similar studies [24].

Following the completion of the greese and dry tests, the samples were employed by an advanced optical profilometer, to capture high-resolution images of the metal's wear track and scar depth profiles.

This process was imperative to obtain precise and accurate results. The wear track values were determined through a careful analysis of the profilometry images. The obtained results for both types of tests are presented in Figures 20 and 21.

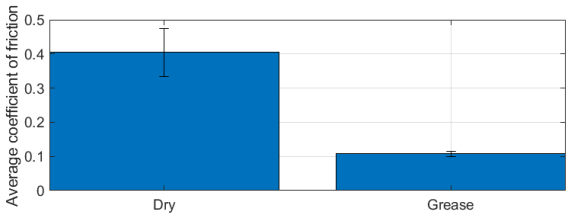

Figure 19 – Average CoF for the dry and grease tests.

a) 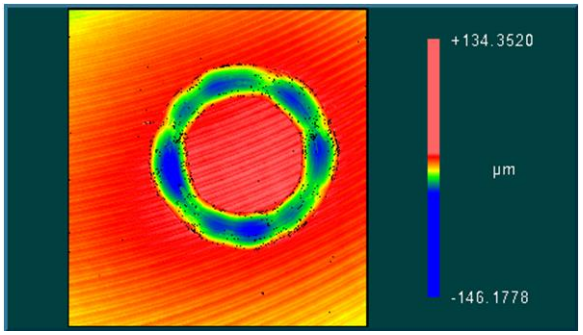

b) 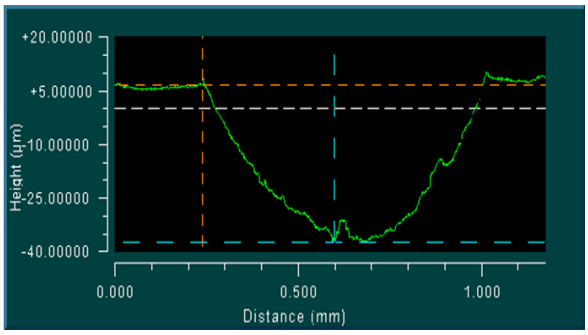

Figure 20 – Example of the optical profilometry image (a) and scar depth profile (b) for the dry test.

a) 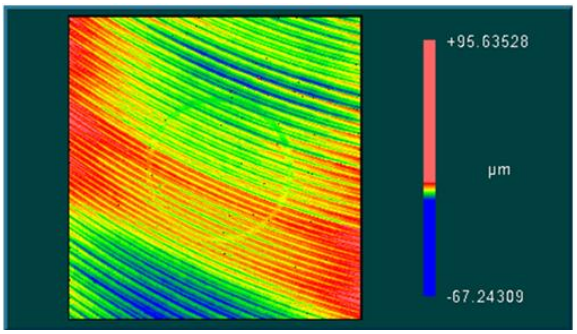

b) 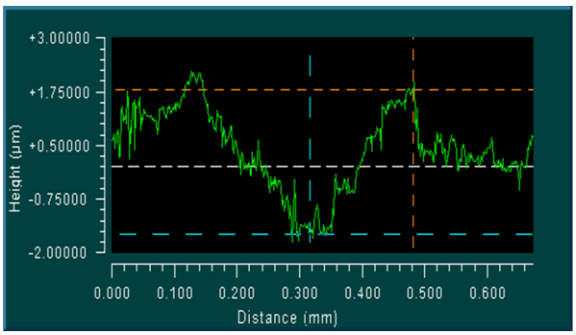

Figure 21 – Example of the optical profilometry image (a) and scar depth profile (b) for the greased test.

The optical profilometry images for the dry test (Figure 20a) revealed that the average wear track width, w_d, was $43.8\mu m$ (Figure 20b). The average track radius, r_t, was revealed from the scar depth profile and was found to be $41.7\mu m$. According to (22), the amount of the wear volume is then

$$\Delta V_{dry} = \frac{\pi r_t w_d^3}{6 r_b} = \frac{\pi \cdot 41.7 \cdot 10^{-3} \cdot \left(43.8 \cdot 10^{-3}\right)^3}{6 \cdot 1.5 \cdot 10^{-3}} = 0.00122\ mm^3 \quad (24)$$

Using (23) for the load (P) of $5N$ and rolling distance (s) of $113.1m$, the CoW of the dry metal was then computed as

$$k_{dry} = \frac{\Delta V_{dry}}{Ps} = \frac{0.00122}{5 \cdot 113.1} = 2.16 \cdot 10^{-6}\ \frac{mm^3}{N \cdot m} = 106 \cdot 10^{-10}\ \frac{in^3 \cdot min}{ibf \cdot ft \cdot h} \quad (25)$$

This result is comparable to the CoW of sintered bronze ($102 \cdot 10^{-10}\ \frac{in^3 \cdot min}{ibf \cdot ft \cdot h}$) [25]. (The latter bushing material is the most similar to the material used in this study.)

Similarly, for the grease test, the optical profilometry images (Figure 21a) revealed the average wear track width of $3.77\mu m$ (Figure 21b). The scar depth profile happened to be r_t=$3.75\mu m$. The wear volume then was evaluated as

$$\Delta V_{grease} = \frac{\pi r_t w_d^3}{6 r_b} = \frac{\pi \cdot 3.75 \cdot 10^{-3} \cdot \left(3.77 \cdot 10^{-3}\right)^3}{6 \cdot 1.5 \cdot 10^{-3}} = 70 \cdot 10^{-9}\ mm^3 \quad (26)$$

Assuming the previous sample values of the load and rolling distance, the CoW for the grease metal is

$$k_{grease} = \frac{\Delta V_{dry}}{Ps} = \frac{70 \cdot 10^{-9}}{5 \cdot 113.1} = 1.24 \cdot 10^{-10} \frac{mm^3}{N \cdot m} = 60 \cdot 10^{-14} \frac{in^3 \cdot min}{ibf \cdot ft \cdot h} \quad (27)$$

Comparing (25) and (27), it becomes clear that a fully greased bushing reduces wear by four orders of magnitude, which is consistent with the previous results as well [26].

11. DT Tuning

Once the main LG DT was developed, the tuning process took place to verify its validity via comparing its outputs with available data on the drag brace obtained over the course of many years from a variety of projects. This database consists of bushing wear measured once at the end of the operational life (see Figure 1). Figure 22a shows a typical dependence of the bushing size as a function of the number of flights (take-offs and landings) for bushing upper (see Figure 4b).

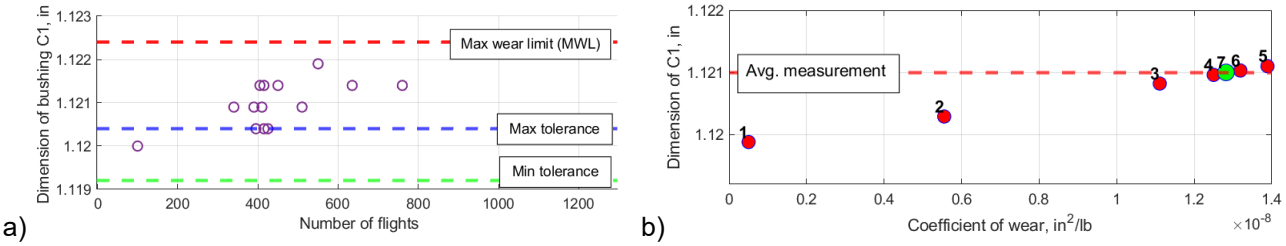

Figure 22 – C1 bushing measurements history (a) and DT tuning results (b).

At this time, the DT tuning involved a single varied parameter, CoW, with an objective of having bushing of 1.121*in* after around 400 sorties as observed in Figure 22a. Figure 22b illustrates the tuning results. Optimization assumed an average operational conditions and the initial bushing dimension of 1.1198*in*. The initial CoW value was set as $0.14 \cdot 10^{-10} in^2 lb^{-1}$ and the "tuned" value corresponding to Figure 22b happened to $1.28 \cdot 10^{-8} in^2 lb^{-1}$.

With this tuned CoW value more experiments were conducted to explore the effect of initial bushing wear and effect of the sink rate at touchdown. To this end, Figure 23 illustrates the wear rate per flight over the lifespan of the bushing. As the bushing becomes more worn and the clearance in contact with the pin increases, the wear rate also rises. This is due to the increase in stress and displacement magnitude with larger clearance. Consequently, it can be inferred that the wear rate of the bushing follows an exponential growth.

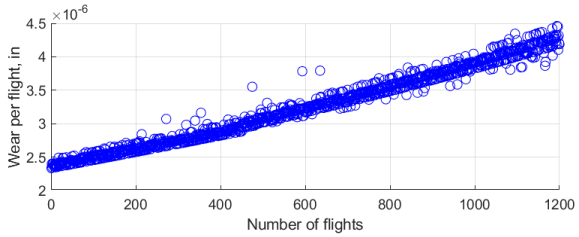

Figure 23 - Wear per flight over bushing lifespan.

Figure 24a shows how the initial bushing size affects the maintenance decision. When bushing starts at the maximal tolerance limit (minimal bushing material) of 1.1204*in*, it reaches MWL after only 570 flights (under average operational conditions). In contrast, starting operations at the minimal tolerance limit (maximum material) of 1.1192*in* extends the wear life 1.8 times, up to 1,030 flights.

With simulations staring at the same wear level of 1.1198*in*, proficient aircraft operations (ensuring soft landings) result in 800 landings before reaching MWL (Figure 24b). Hard landings shorten the lifespan by 19%, down to 670 landings.

To conclude the analysis of the developed and tuned LG DT, Table 1 shows contributions of taxi braking, landing, and retraction gear operations on the overall bushing wear for one aircraft sortie

(based on a simulation conducted under normal operational conditions with an initial bushing size of 1.1198*in*).

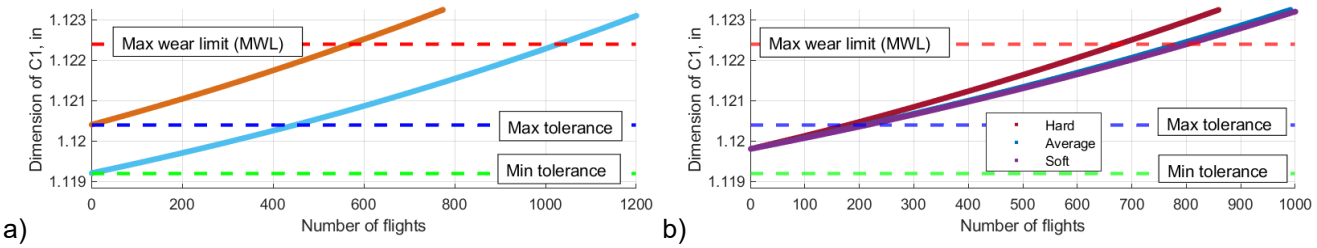

a) b)

Figure 24 – Effects of wear measurement accuracy (a) and operational conditions (b).

Table 1 data indicates that the most significant factor affecting bushing wear happens to be LG retraction and extension (46% combined). This observation seems to be logical given the full range of bushings movement, which is the key parameter influencing the wear rate. It can also be observed that the taxi braking has as great impact as LG extension (31%) and exceeds that of touchdown (22%).

Table 1. Bushing wear during the different phases of flight.

Phase	Designation in Figure 5	Wear per sortie, *in*	Proportion, %
Retraction	R	$4.6 \cdot 10^{-7}$	15%
Extension	E	$9.5 \cdot 10^{-7}$	31%
Landing	L	$6.9 \cdot 10^{-7}$	22%
Braking	B	$9.5 \cdot 10^{-7}$	31%
Total		$3.05 \cdot 10^{-6}$	100%

12. DT Interface

This section illustrates the essence of the developed DT in operation using the user interface (UI) enabling a user to monitor the lifespan of bushings in the drag brace. The DT app was developed in MATLAB utilizing the App Designer tool. The app resides on a computer with a network connection allowing to access flight data repository cloud.

Upon accessing the main home tab, the user selects the tail number of the aircraft he wishes to analyse (Figure 25 shows a fragment of a home tab). The DT UI then lists all flights performed by this aircraft that have yet to be analysed. The user initiates the analysis by pressing the 'run' button, prompting the DT to compute wear and update the predicted state of bushing.

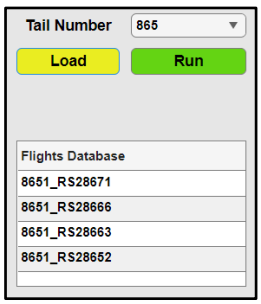

Figure 25 – The home tab of the developed DT app.

For each flight, a separate tab can be opened displaying a dashboard divided into four partitions (Figure 26): touchdown performance (in the upper-right), braking performance (in the lower-right), estimate of the touchdown loads (in the upper-left), and wear rate analysis (in the lower-left). Most of the charts have been discussed/presented in the previous sections already.

The dashboard also features two indices utilised to visualise landing and braking harnesses. The first one, to be found in the in the upper-right quadrant, is computed based on the aircraft weight, sink rate,

and touchdown speed. The second one, see in the lower-right quadrant, depends on the aircraft weight and deceleration rate.

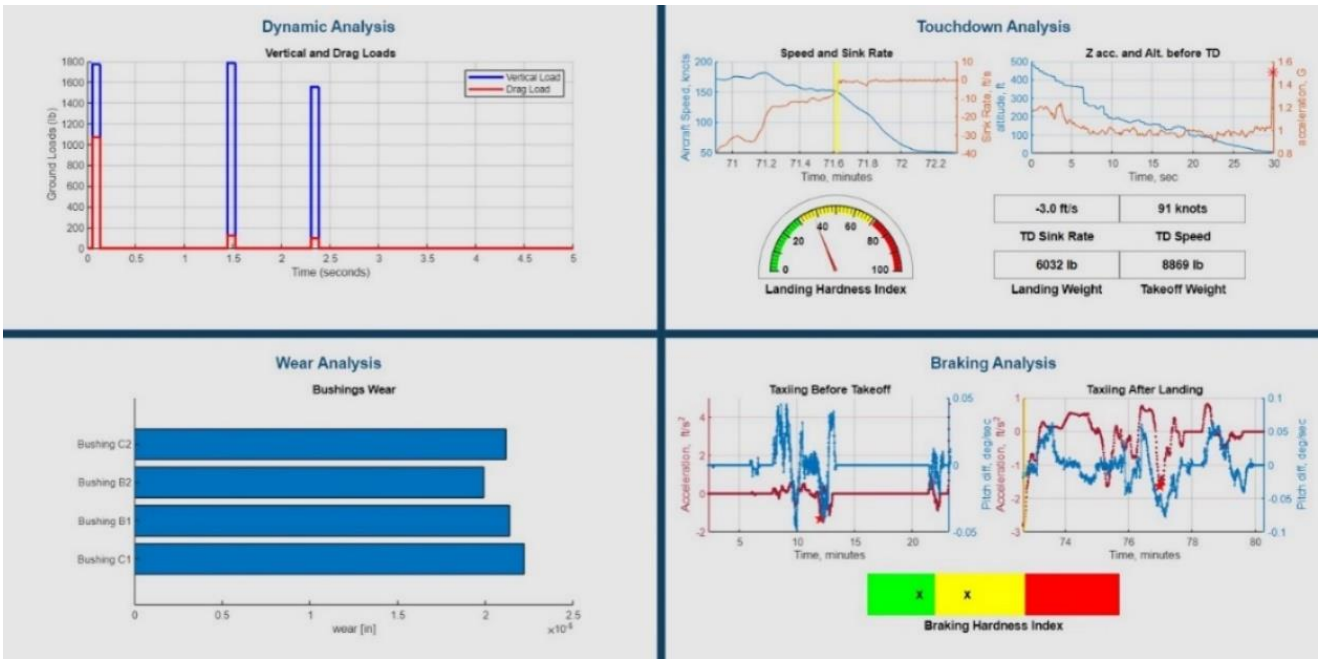

Figure 26 – Individual flight wear-analysis dashboard.

Upon completion of each flight analysis, the dimensions of the main bushings are saved, and the next flight commences with these new bushing estimates as the initial condition.

Another tab of the DT UI shows the summary for a chosen aircraft providing the most up-to-date estimate on bushings wear and remaining safe-operation lifespan to reach the maximum wear threshold (Figure 27).

Figure 27 – Individual aircraft LS bushing health monitoring tab.

A similar tab then shows this information for the entire squadron to assist in maintenance decision making.

13. Conclusion

This research addressed the development and integration of the DT technology into the aircraft LG system maintenance, emphasizing the transformative impact of this advanced tool on operational reliability and enabling predictive maintenance. By deploying a digital replica that dynamically mirrors a main LG of F-16, this paper leveraged real-time data alongside sophisticated simulations to predict bushing wear and remaining lifespan, optimize maintenance schedules, and extend the LG component's operational life. The developed DT utilises multiple interconnected models to include flight data analysis model that processes vital parameters from aircraft computers to provide information about touchdown and taxing performance, dynamic load model trained to predict the LG loads depending on a specific flight configuration and landing hardness, and bushing wear model to quantify wear rates under various environmental conditions. The developed DT was successfully aligned with and verified by the existing extensive database and has already allowed to do several discoveries to include a relative contribution of different processes to bushing wear; the effect of the LG retraction-extension, sharp braking events, landing intensity, and other critical operational parameters; the impact of bushing size measurement accuracy, bushing clearance, and lubrication. The developed DT has been assessed as technologically mature and is now being tested in the real-world environment.

14. Acknowledgement

The authors are thankful to the Engineers and Scientists Exchange Program (ESEP) run by the Navy International Programs Office for supporting this research. ESEP is a professional development program aimed at promoting international cooperation in military research, development, testing and evaluation communities through the exchange of practical experience of defence engineers and scientists.

15. Author Email Addresses

Capt. Sabag: David_sabag@idf.il
Prof. Yakimenko: oayakime@nps.edu
Major Alian: Hasib.Elian@idf.il

16. Copyright Statement

References

[1] General services administration Federal Acquisition Service, Region 8. "Request for Information: F-16 Drag Brace Study." Great.gov.uk, www.great.gov.uk/export-opportunities/opportunities/request-for-information-f16-drag-brace-study. Accessed 9 May 2024.

[2] Siddall S. F-16 drag brace study. F-16.net, 8 Aug. 2002. www.f-16.net/f-16-news-article1030.html#google_vignette. Accessed 9 May 2024.

[3] Hanief M and Charoo M. Archard's wear law revisited to measure accurate wear coefficient considering actual sliding velocity. Materials Today: Proceedings. Vol. 47, pp. 5598-5600, 2021.

[4] Digital twin assessment, agile verification processes, and virtualization technology. Office of the Director Operational Test and Evaluation, Washington D.C. July 2022.

[5] Achouch M, Dimitrova M, Ziane K, Sattarpanah Karganroudi S, Dhouib R, Ibrahim H, Adda M. On Predictive maintenance in industry 4.0: Overview, models, and challenges. Applied Sciences. Vol. 12, No. 16, Article 8081, 2022.

[6] Zaccaria V, Stenfelt M, Aslanidou I and Kyprianidis K. fleet monitoring and diagnostics framework based on digital twin of aero-engines. Proceedings of the ASME Turbo Expo 2018: Turbomachinery Technical Conference and Exposition. Vol. 6, 2018.

[7] Bickford J, Bossuyt D L, Beery P and Pollman A. Operationalizing digital twins through model-based systems engineering methods. Systems Engineering INCOSE. Vol. 23, No. 6, pp. 724-750, 2020.

[8] Gaikwad A, Sambhe R and Ghawade P. Modeling and analysis of aircraft landing gear: Experimental Approach. International Journal of Science and Research. Vol. 2, No. 7, pp.366-369, 2013.
[9] Schonauer S. F-16 Fighting Falcon News. accessed September 26, 2023. www.f-16.net/news_article3472.html. Accessed 9 May 2024.
[10] F-16 drag brace discussion. F-16.net, 20 Jan. 2017. www.f-16.net/forum/viewtopic.php?f=23&t=53779. Accessed 9 May 2024.
[11] Liu Z, Meyendorf N and Mrad N. The role of data fusion in predictive maintenance using digital twin. AIP Conference Proceedings. Vol. 1949, 2018.
[12] Brandt SA., Stiles RJ, Bertin JJ and Whitford R. Introduction to aeronautics: A design perspective. 3rd edition, AIAA, 2025.
[13] PD V0.21/Asm4 0.50.2: Reverse engineering the F16 main landing gear, forum.freecad.org/viewtopic.php?t=78962. Accessed 9 May 2024.
[14] Wu P. A physics-based approach to assess critical load cases for landing gears within aircraft conceptual design. Doctoral Dissertation, Delft University of Technology, 2019.
[15] Devaraju A. A critical review on different types of wear of materials. International Journal of Mechanical Engineering and Technology. Vol 6, No. 11, pp.77-83, 2013.
[16] Dickrell D. J. and Sawyer W. G. Evolution of wear in a two-dimensional bushing. Tribology Transactions. Vol. 47, No. 2, pp. 257-262, 2004.
[17] Endo K and Goto H. Effects of environment on fretting fatigue. Wear. Vol. 48, No. 2, pp. 347-367, 1978.
[18] Koh Y, Park K, Lee H and Kang K. Influence of tibiofemoral congruency design on the wear of patient-specific unicompartmental knee arthroplasty using finite element analysis. Bone Joint Research. Vol. 8, No. 3, pp. 156-164, 2019.
[19] Gao X, Fan L, Dong L, Hu X. Analytical and numerical investigation on contact pressure distribution and deformation of cylindrical roller thrust bearings under various loading conditions. Advances in Mechanical Engineering. Vol. 14, Issue 6, 2022.
[20] C63000 Bronze vs. C63200 Bronze. MakeitForm.com. accessed November 21, 2023.
[21] Mobilgrease 28, ExxonMobil Aviation, accessed December 26, 2023. www.exxonmobil.com/en/aviation/mobilgrease-28.
[22] Standard test method for wear testing with a pin-on-disk apparatus. ASTM International. pp. 1-5, 2004.
[23] Kulkarni A, Rice S, Ansell T. Enhancing mechanical and tribological properties of coldsprayed aluminum through graphene nanoplatelet and boron carbide reinforcement. Journal of Thermal Spray Technology. Vol. 32, pp. 2351-2363, 2023.
[24] Carvalho A C, Rezende A B, Fernandes F M, Miranda R S, Kina E J, Cousseau T and Mei P R. Effect of grease viscosity and thickener on the wear resistance of a class D railway wheel. Wear. Vol. 530-531, pp. 204544, 2023.
[25] Budynas RG and Nisbett JK. Shigley's mechanical engineering Design. 8th edition. McGraw-Hill, 2008.
Wang L, Lewis R, Evans M, Liu Z. Influence of different application of lubricants on wear and pre-existing rolling contact fatigue cracks of rail materials. Tribology Letters, Vol. 65, No. 3, pp. 58, 2017.